Journal of Translational Medicine

RESEARCH

Open Access

Engineered microparticles modulate arginine metabolism to repolarize tumor-associated macrophages for refractory colorectal cancer treatment

Jun Wang[1†], Shenghe Deng[2†], Denglong Cheng[1†], Junnan Gu[1], Le Qin[1], Fuwei Mao[1], Yifan Xue[1], Zhenxin Jiang[1], Mian Chen[1], Falong Zou[1], Ning Huang[1], Yinghao Cao[3,4,5*] and Kailin Cai[1*]

Abstract

Background Arginase is abundantly expressed in colorectal cancer and disrupts arginine metabolism, promoting the formation of an immunosuppressive tumor microenvironment. This significant factor contributes to the insensitivity of colorectal cancer to immunotherapy. Tumor-associated macrophages (TAMs) are major immune cells in this environment, and aberrant arginine metabolism in tumor tissues induces TAM polarization toward M2-like macrophages. The natural compound piceatannol 3′-*O*-glucoside inhibits arginase activity and activates nitric oxide synthase, thereby reducing M2-like macrophages while promoting M1-like macrophage polarization.

Methods The natural compounds piceatannol 3′-*O*-glucoside and indocyanine green were encapsulated within microparticles derived from tumor cells, termed PG/ICG@MPs. The enhanced cancer therapeutic effect of PG/ICG@MP was assessed both in vitro and in vivo.

Results PG/ICG@MP precisely targets the tumor site, with piceatannol 3′-*O*-glucoside concurrently inhibiting arginase activity and activating nitric oxide synthase. This process promotes increased endogenous nitric oxide production through arginine metabolism. The combined actions of nitric oxide and piceatannol 3′-*O*-glucoside facilitate the repolarization of tumor-associated macrophages toward the M1 phenotype. Furthermore, the increase in endogenous nitric oxide levels, in conjunction with the photodynamic effect induced by indocyanine green, increases the quantity of reactive oxygen species. This dual effect not only enhances tumor immunity but also exerts remarkable inhibitory effects on tumors.

Conclusion Our research results demonstrate the excellent tumor-targeting effect of PG/ICG@MPs. By modulating arginine metabolism to improve the tumor immune microenvironment, we provide an effective approach with clinical translational significance for combined cancer therapy.

Keywords Arginase, Nitric oxide, Tumor-associated macrophages, Cancer therapy

†Jun Wang, Shenghe Deng and Denglong Cheng contributed equally to this work.

*Correspondence:
Yinghao Cao
yinghaocao@hust.edu.cn
Kailin Cai
caikailin@hust.edu.cn
Full list of author information is available at the end of the article

Introduction

Research conducted over the past few decades has revealed a close relationship between malignant tumors and the immune system [1]. Immunotherapy has brought hope due to long-term effects on cancer treatment [2]. Nevertheless, the immunosuppressive tumor microenvironment hinders further advances in immunotherapy. Tumor-associated macrophages (TAMs) represent the most abundant immune cells within this environment. TAMs can be classified into two types: M1-like macrophages, which possess tumor-killing abilities, and M2-like macrophages, which promote tumor progression [3]. Numerous studies have demonstrated that dysregulated amino acid metabolism in tumor tissue affects the survival, proliferation, and functional activation of immune cells in the tumor microenvironment [4]. Abnormal arginine metabolism is a key factor leading to TAM differentiation [5, 6]. Modulating arginine metabolism in tumor tissue to increase the M1/M2 ratio in the tumor microenvironment is an effective approach to enhance the effectiveness of immunotherapy.

ARG1 and iNOS are two essential enzymes that play pivotal roles in arginine metabolism in tumor tissues. ARG1 is often overexpressed in tumors [7], where it promots arginine metabolism to produce substances such as ornithine and polyamines, which contribute to the formation of an immunosuppressive microenvironment and induce the polarization of TAMs toward M2-like macrophages [8]. On the other hand, iNOS promotes arginine metabolism to produce nitric oxide (NO), facilitating TAM polarization toward M1-like macrophages [9, 10]. Therefore, simultaneously inhibiting ARG1 activity in tumors while promoting iNOS activity can effectively reduce the proportion of M2-like macrophages, improve the immunosuppressive tumor microenvironment, and boost the effectiveness of tumor immunotherapy [11]. Currently, various drugs targeting arginase have been developed to regulate TAM phenotypes [12, 13]. However, most commonly used inhibitors, such as boronic acid, nor-NOHA, NOHA, and CB-1158, have unclear pathological toxicity, high long-term costs, and issues with complex structural modifications and low drug bioavailability during drug delivery [14–17]. Natural compounds, with advantages such as easy accessibility and controllable toxicity, are gradually becoming favored in nanomedicine delivery. Piceatannol 3′-*O*-glucoside (PG), the main active component of the traditional Chinese herbal medicine rhubarb, possesses multiple functions including anti-inflammatory, antiaging, and immune-enhancing properties [18], and its safety has been extensively validated. In addition to inhibiting arginase activity, PG can also increase the activity of NOS, inhibiting the formation of M2-like macrophages while promoting the polarization of M1-like macrophages [19]. Some studies have reported that PG alone can promote TAM polarization into M1-like macrophages [20]. Therefore, PG is an excellent natural chemical drug with a triple-effect mechanism used to improve arginine metabolism in tumors, promote TAM repolarization into M1-like macrophages, and enhance tumor immunity. Additionally, cells secrete extracellular vesicles (EVs) in response to internal and external stimuli [21]. Among EVs, cell microparticles (MPs), are characterized by diameters ranging from 100 to 1000 nm [22]. Compared with other artificially synthesized nanocarriers, MPs exhibit strong homologous targeting and biological safety, hold immense potential for tumor-targeted drug delivery, and are increasingly recognized as promising drug delivery modalities across a spectrum of diseases [23, 24]. In a phase I trial, Bernard et al. documented the excellent safety of EVs derived from dendritic cells (DCs) in melanoma patients [25]. Furthermore, Benjamin et al. demonstrated in a phase II clinical trial that EVs derived from DCs could increase the antitumor functions of NK cells in patients with non-small cell lung cancer [26]. Hence, the delivery of natural drugs using vesicles has potential for translation into clinical applications.

Here, we report the use of tumor cell-derived MPs for the delivery of two drugs, PG and indocyanine green (ICG), termed as PG/ICG@MPs, for tumor-targeted therapy. ICG, an FDA-approved near-infrared dye, is used in clinical imaging and therapy [27]. After successful delivery to the tumor site, PG within PG/ICG@MPs inhibits arginase activity in tumor tissue, thereby reducing the number of M2-like macrophages. Additionally, PG activates NOS enzymes to promote NO synthesis. Both NO and PG drive the polarization of TAMs to M1-like macrophages to boost tumor immunity. Moreover, under 808 nm laser irradiation, NO synergizes with the photodynamic effect of ICG to generate more reactive oxygen species (ROS) for tumor ablation. In summary, our PG/ICG@MPs display an excellent targeting capability after intravenous injection (Scheme 1). By inhibiting the aberrant metabolism of arginine in tumors and activating tumor immunity, combined with the photodynamic effect of local 808 nm irradiation, remarkable therapeutic effects on tumors have been observed. The successful implementation of this study significantly advances the development of natural drugs with multiple potentials. This property is crucial for reducing the time and cost associated with the clinical translation of immunotherapy.

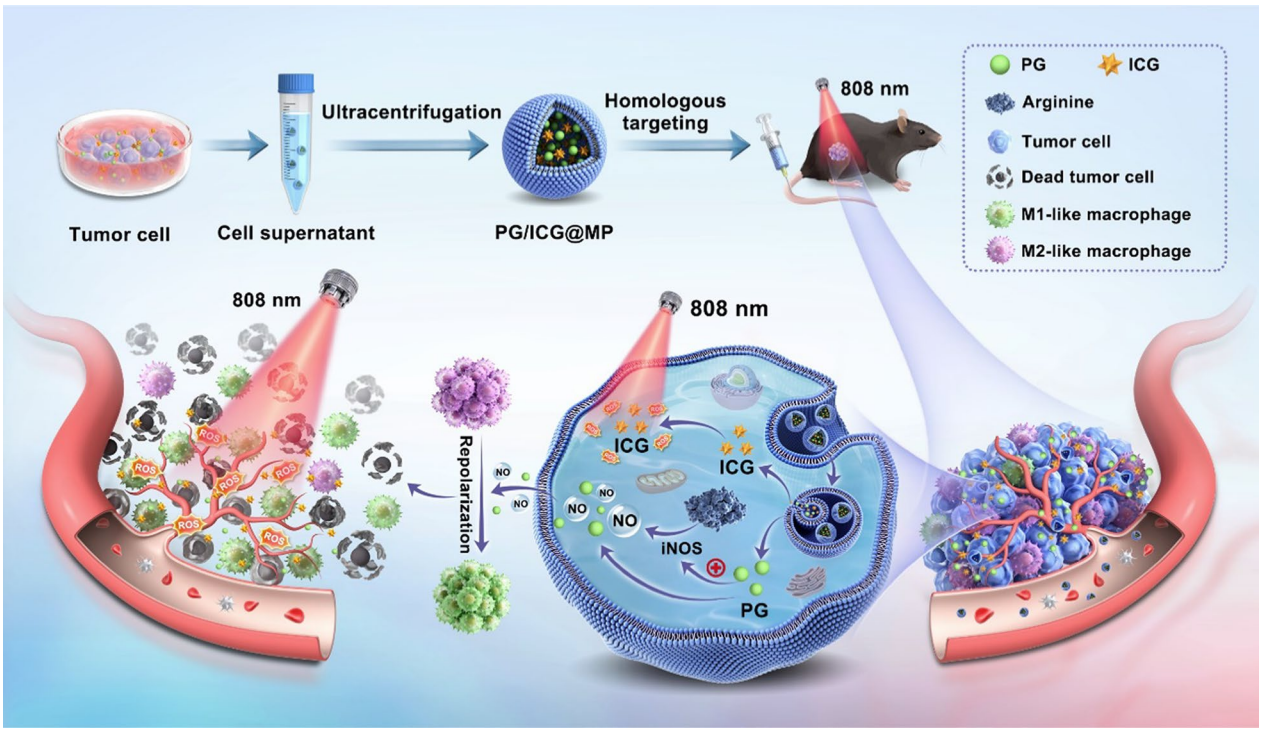

Scheme 1 Schematic illustration of in vivo PG/ICG@MP therapy. PG/ICG@MPs specifically target tumor tissue for the controlled release of PG and ICG. PG facilitates the generation of endogenous NO, effectively polarizing TAMs into M1-like macrophages synergistically with PG. In addition, NO synergizes with the photodynamic effect of ICG to generate more ROS for tumor ablation. By inhibiting abnormal arginine metabolism in tumors to activate tumor immunity and combining with localized 808 nm irradiation, enhanced tumor therapy has been achieved

Materials and methods

Human CRC tissues, cell lines, and ethics statement

The cell lines used in this work were all obtained from the American Type Culture Collection (ATCC, USA) and the National Collection of Authenticated Cell Cultures. The cell culture medium was DMEM (Gibco, MA, USA) or RMPI 1640 (Gibco, MA, USA), supplemented with 10% fetal bovine serum and 1% penicillin/streptomycin. The cells were cultured in a controlled environment (95% air, 5% CO_2, 37 °C).

The colorectal cancer tissue used in this study was handled in compliance with the Code of Ethics of the World Medical Association (Declaration of Helsinki). All patients provided signed informed consent and did not receive adjuvant chemotherapy before surgery. Our research was approved by the Human Research Ethics Committee of Huazhong University of Science and Technology.

Bioinformatic analysis

To analyze the expression levels of ARG1 across various cancers, the UALCAN database was utilized, the "Proteomics" option was selected, and the target gene "ARG1" was entered into the gene input box. The "Pan-cancer view" feature was then employed to visualize ARG1 expression across different cancer types. For specific analysis of colon cancer, the "Colon cancer" option was chosen, followed by selecting the "Total protein" button to retrieve the expression data for ARG1 in this cancer type. Similarly, the GEPIA database (http://gepia.cancer-pku.cn/) was used to assess the expression levels of ARG2. On the GEPIA homepage, "ARG2" was entered into the gene input box, and the search function was activated. In the "Expression DIY" section, the tumor types "Colon adenocarcinoma (COAD)" and "Rectum adenocarcinoma (READ)" were selected to obtain the expression data for ARG2 in colon and rectal cancers. For evaluating ARG2 expression in various tumor cell lines, the Human Protein Atlas (https://www.proteinatlas.org/) was consulted. After entering "ARG2" in the search box on the homepage, the "Cell line" option was selected from the search results to access the relevant expression data. Additionally, the STRING database (https://cn.string-db.org/) was employed to construct a Protein–Protein Interaction (PPI) network for ARG and NOS family proteins. By selecting the "Multiple proteins" option on the homepage and entering "ARG1, ARG2, NOS1, NOS2, NOS3"

into the protein name input box, a comprehensive PPI network map was generated.

Preparation and characterization of PG/ICG@MPs

LoVo, MC38 cells were starved for 12 h, and then exposed to UV irradiation (UVB, 300 J/min) for 1 h. Next, the cells were treated with PG (5 μg/mL) and ICG (10 μg/mL) for 24 h. The supernatants were subsequently centrifuged at 600×*g* for 10 min and 3000×*g* for 15 min to remove debris. Subsequently, the supernatants were centrifuged at 18,000×*g* for 60 min to collect the drug-loaded MPs, after which the pellets were washed three times with PBS. The morphology of the MPs was observed by using a transmission electron microscope (TEM, HT7800). The size and zeta potentials of the drug-loaded MPs were measured via Dynamic Light Scattering (DLS, Zetasizer Nano ZS90, Malvern). The concentration of PG in the MPs was determined using High-Performance Liquid Chromatography (HPLC) with a Hypersil Gold C18 column (250 mm*4.6 mm, 5 μm). The concentration of ICG in MPs was quantified using a UV spectrophotometer (Nanodrop, USA) at 780 nm.

Western blotting and RT-qPCR

For Western blotting, tissues and cells were lysed via ultrasonic disruption with a mixture of RIPA lysis buffer (P0013B, Beyotime), phenylmethylsulfonylfluoride (PMSF, # ST506, Beyotime), and phosphatase inhibitor (HY-K0021, MCE). After 30 min, the supernatant was collected by centrifugation. Protein concentrations were quantified using BCA Protein Assay Kit (KTD3001, Abbkine, China). The proteins were then exposed using a gel imaging system (Bio-Rad, USA) after electrophoresis, membrane transfer, and incubation with primary and secondary antibody. Table S1 shows the primary antibodies used.

A FastPure Cell/Tissue Total RNA Isolation Kit (RC101-01, Vazyme) was used to extract total RNA. Next, the extracted RNA was reverse transcribed to generate cDNA, which was subsequently detected by qPCR utilizing a one-step PCR system. Table S2 shows the sequences of the primers used.

Homologous targeting ability of PG/ICG@MPs in vitro and in vivo

LoVo cells were exposed to PG/ICG@MPs (PG, 40 ng/mL; ICG, 5 μg/mL) for 0, 2, 4, and 8 h, respectively. The intracellular fluorescence was then assessed with a fluorescence microscope (Olympus, IX73, Japan) for both the ICG and LysoTracker. For precise targeted intracellular uptake assays, LoVo cells, SW480 cells, 786O cells, and HUVECs were treated with PG/ICG@MPs for 24 h. The intracellular fluorescence of LysoTracker, ICG, and Hoechst was then detected using a fluorescence microscope (Olympus, IX73, Japan).

Various subcutaneous tumor models were created using MC38, MB49, and RM-1 cells. PG/ICG@MPs derived from MC38 cells and labeled with DiR were subsequently intravenous injected into the mice. After 12 h, the in vivo fluorescence of the subcutaneous tumors in the tumor-bearing mice was detected using a Bruker MI SE 721 imaging system (Bruker, USA).

ARG1 inhibition and iNOS activation of PG/ICG@MPs

LoVo cells were treated with PBS, PG/ICG, or PG/ICG@MP for 24 h, and then illuminated with or without an 808 nm laser. The levels of intracellular NO was subsequently verified using the DAF fluorescence probe (S0019S, Beyotime, China). Total NO levels were detected using the Griess reagent (S0021S, Beyotime, China) after treating LoVo cells with PBS, PG, PG/ICG, and PG/ICG@MP for 24 h. LoVo cells were co-incubated with different concentrations of PG (0, 5, 10, 20, 40, 80 μM) for a period of 24 h, and the total NO was tested using Griess reagent. Moreover, 786O, B16 cells were co-incubated with PG (5 μM), and the total NO concentration was measured with Griess reagent after 24 h.

LoVo cells were co-incubated with PBS, PG, PG/ICG, PG/ICG@MP for 24 h. The ATP content in each group was measured using an ATP detection kit (S0026, Beyotime, China). Similarly, the ATP content was measured in LoVo cells treated with different concentrations of PG (0, 5, 10, 20, 40, 80 μM) for a period of 24 h.

LoVo cells were co-incubated with PBS, PG/ICG, or PG/ICG@MP for a period of 24 h. Subsequently, the cells were irradiated with/without 808 nm laser irradiation. Following this, the LoVo cells were stained with DCFH-DA (S0033S, Beyotime, China) and Hoechst 33342 (C1022, Beyotime, China) to measure the ROS levels in different treatment groups.

Polarization of tumor-associated macrophage in vitro and in vivo

RAW 264.7 cells co-cultured with MC38 cells treated with LPS (100 ng/mL), IL-4 (20 ng/mL), PG/ICG, PG/ICG@MP (PG, 40 ng/mL; ICG 5 μg/mL) for 24 h. Subsequently, RAW 264.7 cells were collected for qRT-PCR to detect M1-like macrophage markers (TNF-α, iNOS) or M2-like macrophage markers (ARG1, MRC1).

The same experimental procedures were used for flow cytometry analysis, RAW 264.7 cells were collected for flow cytometry to detect M1-like macrophage markers (CD 80, 104705, Biolegend) or M2-like macrophage markers (CD 206, 141711, Biolegend).

For in vivo detection, tumor tissues were collected and cut into 2*2 mm pieces, then, incubated with DMEM

media containing Collagenase Type I (1 mg/mL), Collagenase Type IV (1 mg/mL), DNase I (5 μg/mL), and Hyaluronidase (0.4 mg/mL) for 6 h at 37 ℃ with persistent agitation. Next, the cells were collected by centrifugation (300*g*, 5 min), then washed twice with PBS and filtered twice using a 70 μm filter, and then the red blood cells were lysed. The single-cell suspensions were co-incubated with Zombie Aqua™ Fixable Viability Kit (423101, Biolegend) and TruStain FcX™ (anti-mouse CD16/32) Antibody (101319, Biolegend). Subsequently, M1 (CD 80) and M2 (CD 206)-like macrophage markers were detected by flow cytometry (BD, USA).

Animal experiments

C57BL/6 mice (6 weeks old, 18–22 g, male) were purchased from Hubei Biont Biological Technology Co., Ltd. Mice were housed in a room with a 12-h light–dark cycle and a constant temperature of 22 ± 2 °C. The animal experiments were performed according to the guidelines set by the National Research Council's Guide for the Care and Use of Laboratory Animals. The protocol received approval from the Institutional Animal Care and Use Committee at Tongji Medical College, Huazhong University of Science and Technology (Approval number S3366).

MC38 cells ($3*10^6$) suspended in 100 μL of PBS were injected subcutaneously into the right flank dorsal of C57BL/6 mice, and the animals were anesthetized with pentobarbital (0.3%, 50 mg/kg). When the volume of the dorsal tumors reached 100 mm^3, the mice were randomly divided into five treatment groups that were intravenously injected with the following treatments via the tail vein: (I) PG/ICG@MP + 808 nm laser, (II) PG/ICG@MP, (III) PG/ICG, (IV) PBS + 808 nm laser, (V) PBS, PBS (100 μL) and PG/ICG@MP (5 μg/mL, 100 μL) were intravenous injected to mice tail vein. After 12 h of injection, the dorsal tumor of mice in group I and IV was irradiated with 808 nm laser (1 W/cm^2, 10 min), and after 24 h, the procedure was repeated. Tumor size and body weight were measured every 2 days using digital vernier calipers and an electronic scale respectively. Tumor volumes were estimated using the following formula: (tumor length) * (tumor width)^2/2. The Normalized tumor volume was calculated as V/V0, where V0 is the initial tumor volume before treatment. Tumor tissues were removed from the mice (one from each group) after 15 days and stained with hematoxylin and eosin (HE) for histological analysis. M1- or M2-like macrophage markers were detected by immunofluorescence histochemistry. At the conclusion of the survival observation, the tumors from the remaining mice in each group were imaged and measured on an electronic scale.

Statistical analysis

All the results are presented as the means ± SDs. $P < 0.05$ was considered statistically significant. The statistical analysis was conducted using Prism 8.0 software (GraphPad). Multiple comparisons among groups were conducted using either one-way ANOVA or two-way ANOVA. The statistical analysis involved conducting unpaired two-tailed Student's t-tests to compare two groups.

Results

Arginase is abundant in various tumors

Arginine metabolism plays a crucial role in cancer development, and numerous studies have highlighted the elevated abundance of arginase in various tumors. Figure 1A shows higher levels of ARG1 expression in different types of cancer, such as colon cancer, renal cancer, endometrioid cancer, pancreatic cancer, head and neck cancer, and glioblastoma, when compared to normal tissues (https://ualcan.path.uab.edu/index.html). Figure 1C demonstrated the overexpression of ARG2 in various cancer cells (https://www.proteinatlas.org/). Additionally, Fig. 1B and D reveal the overexpression of both ARG1 and ARG2 in colon and rectal cancer (http://gepia.cancer-pku.cn/). IHC staining was conducted on 10 pairs of human colorectal cancer tissues and adjacent normal tissues to provide additional evidence for these findings. Figure 1E indicates a higher abundance of ARG1 in tumor tissues compared to normal tissues, with an IHC score approximately close to 8, whereas the IHC score for normal tissues reached only 3 (Fig. 1F). Fig. S1 also demonstrated the overexpression of ARG1 in colorectal tumor tissues and various cell lines. Moreover, Fig. 1G highlights a strong association between arginase and NOS expression, as NOS is the crucial enzyme to generate NO for cancer therapy. These findings implies that targeting arginase could hold promise for precision cancer treatment (https://cn.string-db.org/).

PG inhibits colorectal cancer progression

Considering the elevated expression of arginase in various tumors, including colorectal cancer, targeting arginase with an inhibitor appears promising for colorectal cancer therapy. PG is a natural small-molecule drug known for its ability to inhibit arginase activity and elevate cellular endogenous NO levels, the 2D chemical structure is shown in Fig. S2. To explore the anticancer potential of PG, SW480, LoVo, and HCT116 cells were treated with PG and PBS. As illustrated in Fig. S3, cells treated with PG exhibited reduced invasion and migration compared with those in the control

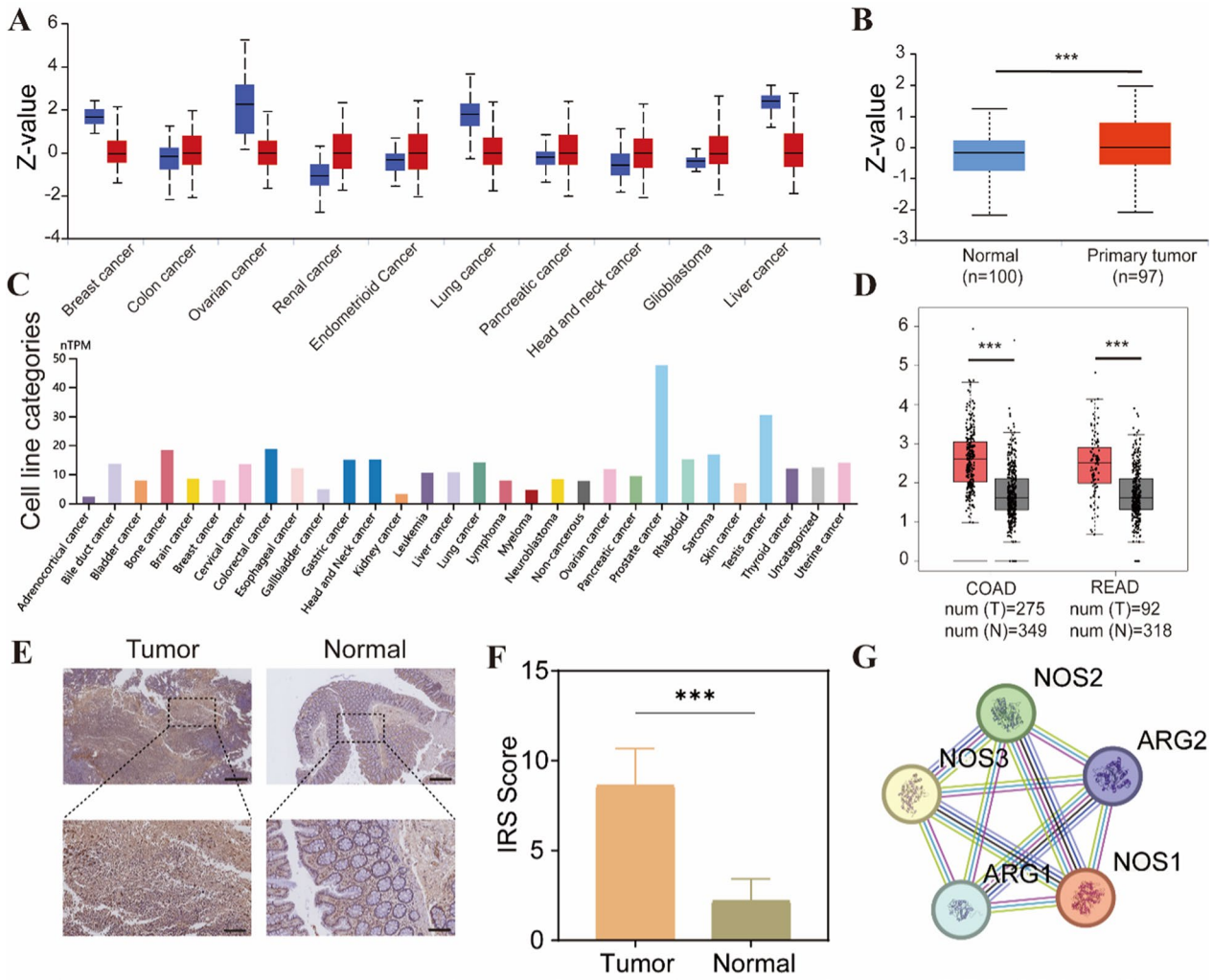

Fig. 1 Arginase is highly expressed in a variety of tumors. **A** The expression levels of ARG1 across various tumors were analyzed using the UALCAN database, with the red bar indicating tumor tissue, and the blue bar indicating normal tissue. **B** The expression levels of ARG1 in colon cancer were analyzed using the UALCAN database. **C** The expression levels of ARG2 in different cancer cell lines were analyzed using THE HUMAN PROTEIN ATLAS database. **D** The expression levels of ARG2 in colon adenocarcinoma (COAD) and rectum adenocarcinoma (READ) were analyzed using the GEPIA database, with the red bar indicating tumor tissue, and the gray bar indicating normal tissue. **E** The expression levels of ARG1 in tumor and normal tissue were assessed via IHC staining. Scale bar: upper picture 200 μm, lower picture 50 μm. **F** Quantification of ARG1 expression levels in tumor and normal tissue from Fig. 1E. **G** A Protein–Protein Interaction (PPI) network of arginase generated using the STRING database. * $p < 0.05$, ** $p < 0.01$, *** $p < 0.001$, **** $p < 0.0001$

group. Additional assays, such as the CCK8 assay and wound healing assay (Fig. S4), further supported the anticancer effects of PG. Besides inhibiting the proliferation, migration, and invasion of tumor cells, PG also promotes tumor cell death. Annexin V-FITC (Fig. S5) and CellTiter-Glo assays (Fig. S6) demonstrated that PG has a stronger tumor-killing effect compared to the control group. In summary, these results suggest that PG has potential as an anticancer drug, and its incorporation into cell microparticles could be explored for cancer therapy.

Preparation and characterization of PG/ICG@MPs

PG/ICG@MPs were collected by gradient centrifugation and quantified using BCA protein analysis. The levels of PG and ICG were analyzed by HPLC and UV–vis spectroscopy, respectively. The PG/ICG@MPs had a drug loading capacity of 3.342 ng of PG and 0.43 μg of ICG per μg of protein. Standard curves for ICG and PG were established using UV spectrophotometry and HPLC (Fig. S7). TEM revealed that PG/ICG@MPs were monodisperse and exhibited a saucer-like morphology (Fig. 2A). Dynamic light scattering (DLS) showed

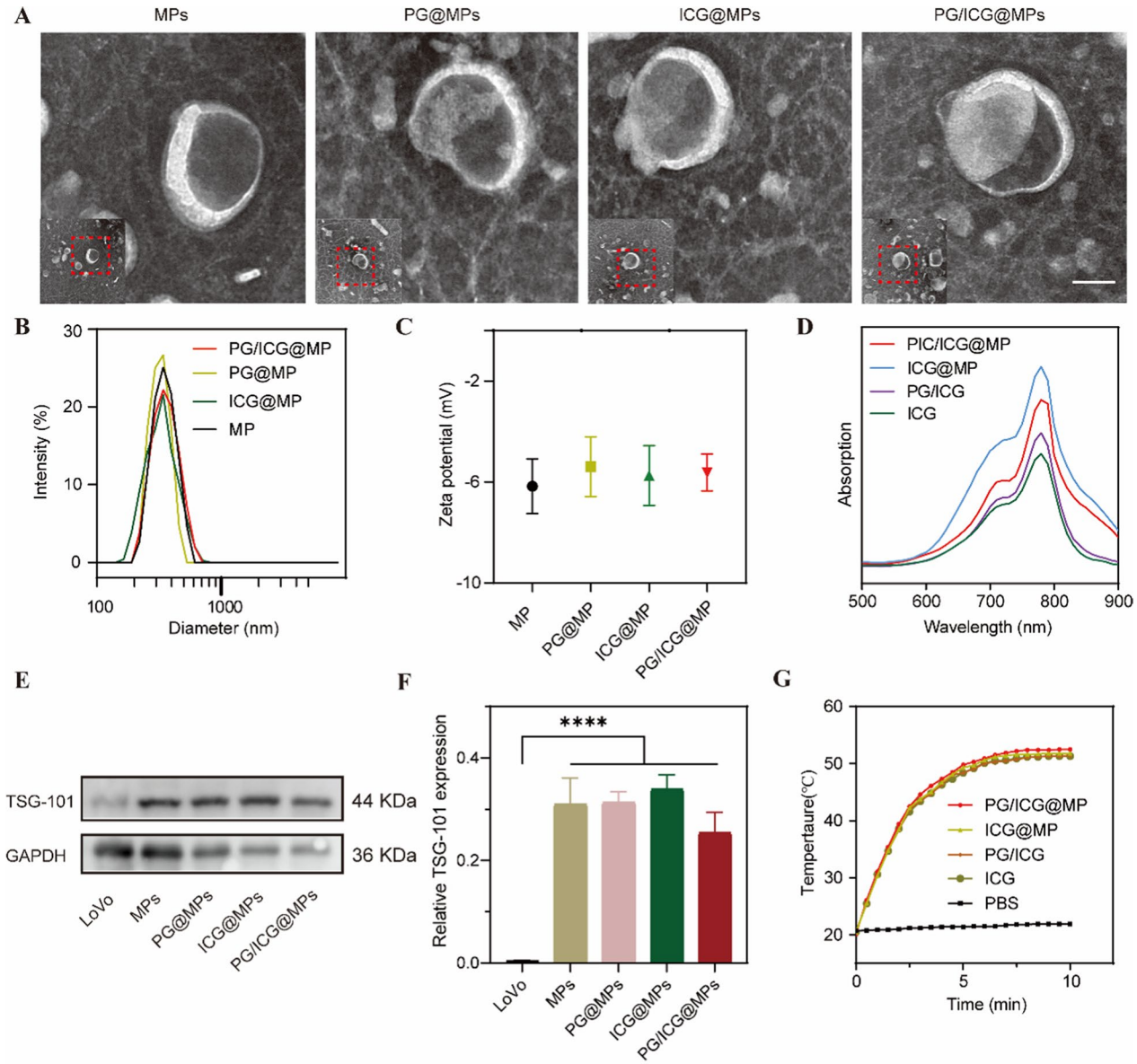

Fig. 2 Characterization of PG/ICG@MPs. **A** TEM images of MPs, PG@MPs, ICG@MPs, and PG/ICG@MPs. Scale bar: 100 nm. **B** Diameters of the MPs, PG@MPs, ICG@MPs, and PG/ICG@MPs determined via DLS analysis (Malvern Zetasizer). **C** Zeta potential of MPs, PG@MPs, ICG@MPs, and PG/ICG@MPs determined via DLS analysis (Malvern Zetasizer). **D** UV—vis spectra of ICG, ICG@MPs, and PG/ICG@MPs. **E** The expression levels of TSG-101 in LoVo cells, MPs, PG@MPs, ICG@MPs, and PG/ICG@MPs were assessed via western blot analysis. **F** Quantification of TSG-101 expression in LoVo cells, MPs, PG@MPs, ICG@MPs, and PG/ICG@MPs. **G** The temperature of PG/ICG@MPs, ICG@MPs, PG/ICG, ICG, and PBS after irradiated with 808 nm laser at different time. * $p < 0.05$, ** $p < 0.01$, *** $p < 0.001$, **** $p < 0.0001$

that the MPs, PG@MPs, ICG@MPs and PG/ICG@MPs exhibited similar morphologies and overall dimensions, with diameters of approximately 350 nm (Fig. 2B) and zeta potentials of -6 mV (Fig. 2C). The UV absorption spectra of ICG, PG/ICG, ICG@MPs, and PG/ICG@MPs were similar, suggesting the effective integration of ICG into the MPs (Fig. 2D). Additionally, to verify the stability of PG/ICG@MPs, we stored them for one week and then measured their particle size and zeta potential to verify their stability (Fig. S8). These results demonstrated the good biostability of PG/ICG@MPs.

TSG-101 is currently recognized as a biomarker of extracellular vesicles, and the purity of our derived microparticles was explored by Western blotting experiments

(Fig. 2E), Fig. 2F presents the quantitative data for TSG-101. In addition, ICG serves as a clinical contrast agent with FDA approval, is commonly employed in liver disease diagnosis [27], and has excellent photothermal and photodynamic therapeutic effects. Figure 2G showcased the strong photothermal characteristics of PG/ICG@MP, ICG@MP, and ICG when exposed to 808 nm laser radiation.

PG/ICG@MPs target tumor tissues precisely to inhibit ARG1 and activate iNOS

Cell microparticles exhibit excellent biocompatibility in vivo, attributed to their homologous targeting ability, making PG/ICG@MPs suitable for precise cancer targeting. In this study, we investigated the cellular uptake and targeting efficiency of PG/ICG@MPs through several fluorescence experiments. Initially, LoVo cell derived PG/ICG@MPs were co-incubated with LoVo cells. Fluorescence microscopy revealed that ICG fluorescence predominantly co-localized with lysosomes, indicating specific internalization via endocytosis. Notably, PG/ICG@MPs entered the intracellular space within 2 h and peaked at 4 h (Fig. 3A), showcasing faster internalization. The fluorescence linear index is presented in Fig. 3C. To evaluate the homologous targeting ability of PG/ICG@MPs, we co-incubated LoVo cell-derived PG/ICG@MPs with various cell lines, including LoVo, SW480, 786O, and HUVECs. After 4 h, cells were washed with PBS three times. Figure 3B illustrates that only LoVo cells exhibited a pronounced green fluorescence, whereas SW480, 786O, and HUVECs did not demonstrate a notable green fluorescence. This indicates that MPs derived from LoVo cells selectively accumulated in LoVo cells, demonstrating excellent targeting ability. To further verify the precise targeting ability of PG/ICG@MPs in vivo, we established subcutaneous tumor models using MB49, RM-1, and MC38 cells. Upon reaching a tumor volume of approximately 100 mm^3, MC38 cell-derived PG/ICG@MPs labeled with DIR fluorescence were intravenously injected. After 12 h, in vivo fluorescence conducted by Caliper IVIS Lumina II (Fig. 3D and E) revealed strong fluorescence exclusively in the MC38 subcutaneous tumor model, consistent with the findings from the previous cell experiments. To further validate the homologous targeting ability in vivo, we assessed the fluorescence of the MC38 subcutaneous tumor model at 0, 6, 12, 24, and 48 h (Fig. S9). The mice were sacrificed at 12 h post-injection, and examination of the relevant internal organs revealed that the fluorescence in the tumor was significantly higher than in other organs (Fig. S10). These finding demonstrates the excellent targeting ability of PG/ICG@MPs.

The successful delivery of PG/ICG@MPs to the targeted tumor tissue prompted a further investigation into their ability to reverse metabolic reprogramming. As illustrated in Fig. 3F, treatment with PG, PG/ICG, PG@MPs, and PG/ICG@MPs were found to decrease ARG1 levels and enhance iNOS levels. Tumor cells were treated with five different groups, including PBS, PBS + laser (PBS + L), PG combined with ICG (PG/ICG), PG/ICG@MP, and PG/ICG@MP + laser (PG/ICG@MP + L). The mRNA levels of ARG1 and iNOS were measured using qPCR, as shown in Fig. 3G and H. The PG/ICG@MP + L treatment exhibited the most significant effects on decreasing ARG1 and increasing iNOS expression.

PG/ICG@MP inhibits cancer progression by generating NO and ROS

As iNOS is a Nitric Oxide synthase, it plays a pivotal role in the promotion of NO production. The accumulated NO levels were quantified using the Griess assay, with the standard curve obtained from the kit (Fig. S11). Figure 4A demonstrated that PG/ICG@MP exhibited the highest NO production, whereas the PBS group showed minimal NO generation. DAF-FM DA is a fluorescent probe that interacts with intracellular nitric oxide, Fig. 4B, C showcased that PG/ICG, PG/ICG@MP, and PG/ICG@MP+L group exhibited higher fluorescence intensity compared to PBS and ICG@MPs after 24 h co-incubation, suggesting that PG/ICG@MP has the potential to enhance intracellular NO generation. Given that PG can activate endothelial nitric oxide synthase by inhibiting arginase, we further explored whether PG also promoted NO production in other tumor cells. Co-incubation of B16, and 786O cells with PG (10 μM) for 24 h, as shown in Fig. S12, PG treated group showed increased NO levels. This suggests that tumors expressing high levels of Arginase may benefit from the therapeutic potential of PG/ICG@MP.

Given that PG/ICG@MPs effectively inhibited arginase activity and promoted NO production, the subsequent objective was to assess the anticancer potential of NO. Previous research has highlighted the significance of NO as a key molecule influencing mitochondrial respiratory metabolism [28]. Elevated NO levels contribute to mitochondrial dysfunction, resulting in diminished ATP production and subsequently lowering cellular energy levels. This phenomenon can be utilized to improve the effectiveness of photodynamic therapy. The functional state of mitochondria can be assessed by measuring alterations in mitochondrial membrane potential (MMP). A JC-1 assay kit was employed to monitor alterations in MMP. JC-1 aggregates and emits red fluorescence when the MMP is high, indicating normal mitochondrial function. On the other hand,

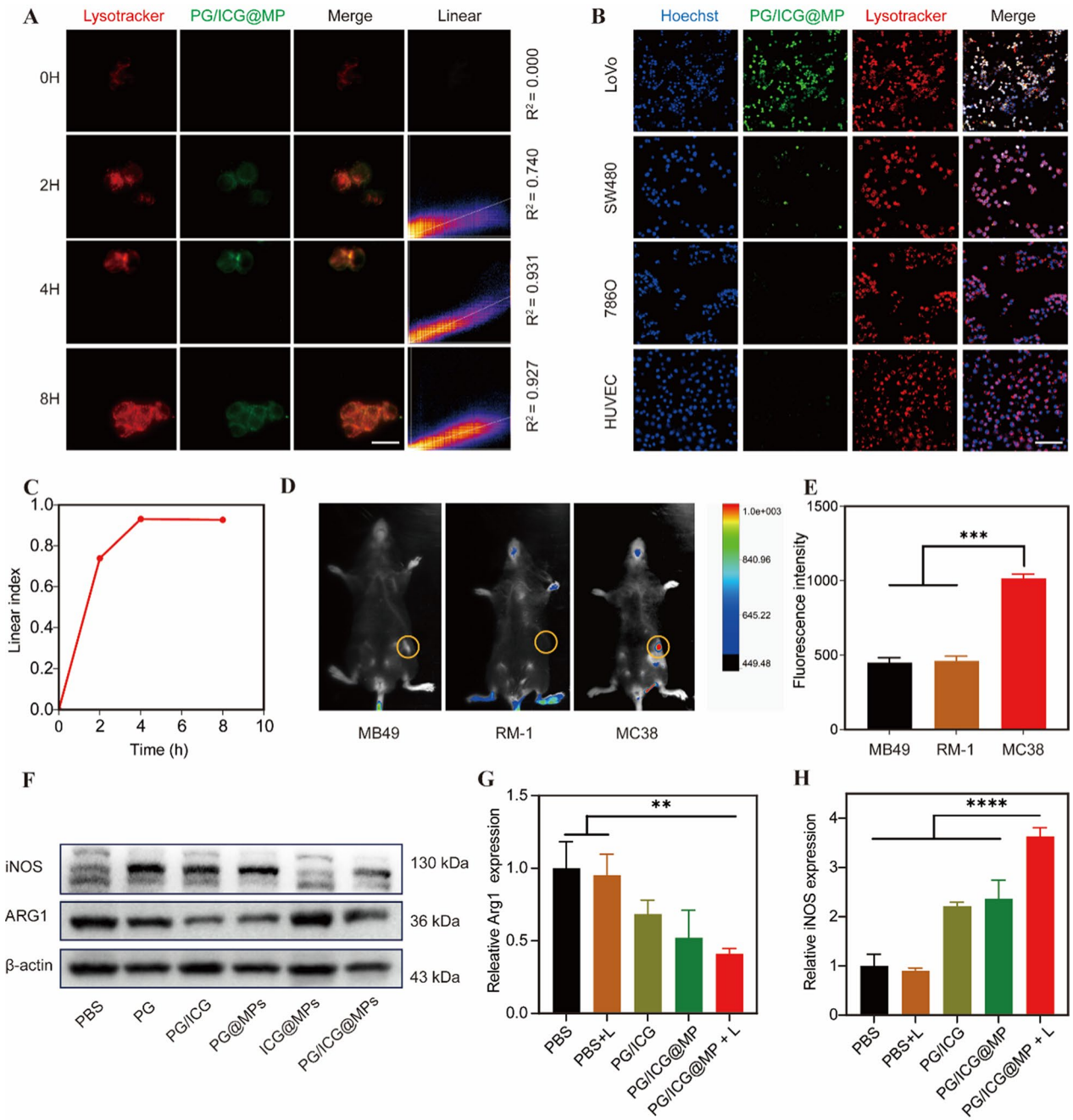

Fig. 3 PG/ICG@MP targets tumor cells to inhibit ARG1 and promote iNOS. **A** The endocytic uptake of PG/ICG@MPs at various incubation times was determined using fluorescence microscopy. Red: lysosomes stained by LysoTracker Red. Green: fluorescence of ICG in PG/ICG@MPs. Scale bar = 20 μm. **B** The specific targeting ability of PG/ICG@MPs across different cell lines was assessed via fluorescence microscopy. Blue: Nuclei stained by Hoechst 33342. Green: Fluorescence of ICG in PG/ICG@MPs. Red: lysosome stained by Lysotracker red. Scale bar = 200 μm. **C** Fluorescence linear index in different time intervals from **A**. **D** In vivo fluorescence of MB49, RM-1, and MC38 subcutaneous tumor mouse model detected by Bruker MI SE 721, n = 3. **E** Quantification of fluorescence intensity in the MB49, RM-1, and MC38 subcutaneous tumor models. **F** The expression levels of iNOS and ARG1 in different treatment groups were detected by western blot analysis. **G**, **H** The expression levels of ARG1 and iNOS mRNAs in different treatment groups were detected using RT-qPCR. * $p < 0.05$, ** $p < 0.01$, *** $p < 0.001$, **** $p < 0.0001$

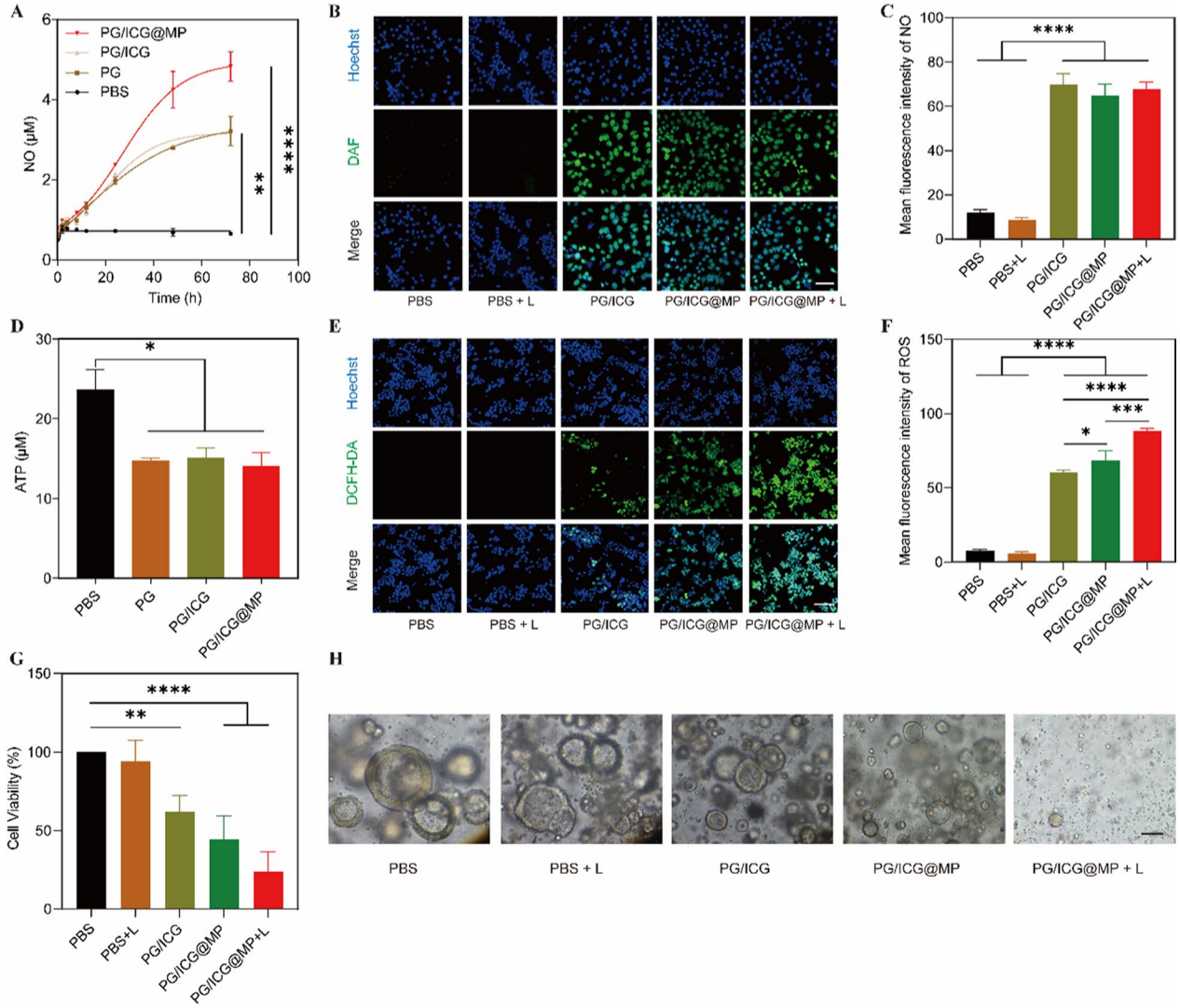

Fig. 4 PG/ICG@MPs promote NO production to inhibit mitochondrial function and enhance ROS production. **A** Cumulative NO release from the PBS, PG, PG/ICG, and PG/ICG@MP groups detected by the Griess assay. **B** Endothelial NO levels in cells treated by PBS, PBS + L, PG/ICG, PG/ICG@MP, and PG/ICG@MP + L groups were detected via fluorescence microscopy. Scale bar = 200 μm. **C** Quantification of the mean fluorescence intensity of NO in **B**. **D** ATP levels in cells treated with PBS, PG, PG/ICG, and PG/ICG@MP group. **E** ROS levels in PBS, PBS + L, PG/ICG, PG/ICG@MP, and PG/ICG@MP + L treatment groups were detected via fluorescence microscopy. Scale bar = 200 μm. **F** Quantification of the mean fluorescence intensity of ROS in the PBS, PBS + L, PG/ICG, PG/ICG@MP, and PG/ICG@MP + L treatment groups. **G** Cell viability in the PBS, PBS + L, PG/ICG, PG/ICG@MP, and PG/ICG@MP + L treatment groups were detected by the CCK8 assay. **H** Photograph of colorectal cancer patient-derived organoids after treatment with PBS, PBS + L, PG/ICG, PG/ICG@MP, and PG/ICG@MP + L. The PG/ICG@MP + L treatment group shows the strongest killing effect. Scale bar = 100 μm. * $p < 0.05$, ** $p < 0.01$, *** $p < 0.001$, **** $p < 0.0001$

JC-1 is present in its monomeric form and emits green fluorescence under conditions of low MMP. Cells were treated with PBS, PG/ICG, PG/ICG@MP, and PG/ICG@MP + L for 24 h, followed by a JC-1 assay. Fig. S13 illustrates that the PG/ICG, PG/ICG@MP, and PG/ICG@MP + L treatment groups all exhibited a reduction in mitochondrial membrane potential, characterized by increased green fluorescence and reduced red fluorescence, indicating MMP depolarization.

Previous studies have highlighted NO as an effective modulator capable of reducing ATP levels by diminishing MMP and fostering mitochondrial dysfunction [29]. Hence, we hypothesized that PG/ICG@MP might impede ATP synthesis. A calibration curve for ATP (Fig. S14) was employed to assess ATP production in various treatment groups. Figure 4D reveals that ATP levels decreased upon co-incubation with PG, PG/ICG, and PG/ICG@MP, while the control group maintained

relatively high ATP levels. Moreover, ATP concentration gradually decreased with increasing PG concentration (Fig. S15), indicating the significant efficacy of PG in decreasing ATP production in cancer cells. The reductions in mitochondrial membrane potential and ATP production, both indicative of mitochondrial dysfunction, results in a reduction in intracellular oxygen consumption. As photodynamic therapy (PDT) efficacy is substantially influenced by the oxygen and NO contents within tumor tissues, the NO generation stimulated by PG/ICG@MPs could enhance PDT treatment efficiency. Subsequently, PDT efficacy was evaluated in different treatment groups using a DCFH-DA fluorescent probe. Figure 4E, F illustrates that PG/ICG@MPs, coupled with 808 nm laser irradiation, exhibited the highest fluorescence intensity compared to other treatment groups. This observation suggests that PG/ICG@MPs promote NO generation, thereby enhancing PDT efficacy.

Subsequently, to evaluate the tumor-killing potential of PG/ICG@MPs, we divided LoVo cells and MC38 cells into five different treatment groups, including PBS, PBS + L, PG/ICG, PG/ICG@MP, and PG/ICG@MP + L. Figure 4G illustrates that the LoVo cell viability of the PG/ICG@MP with laser treatment group reached the lowest, showcasing the most potent killing effect, while the cell viability of the control group reached nearly 100%, Fig. S16 also verified the tumor-killing effects of PG/ICG@MP with 808 nm laser on MC38 cells. Additionally, live and dead cell staining was employed to corroborate the therapeutic killing efficacy of the diverse treatments (Fig. S17). To better mimic the human tumor environment, we established a colorectal cancer patient-derived organoid model. Under different treatment groups (PBS, PBS + L, PG/ICG, PG/ICG@MP, and PG/ICG@MP + L), the growth trends of the organoids varied. The PG/ICG@MP + L group showed the most significant growth inhibition of the organoids (Fig. 4H).

PG/ICG@MPs repolarize TAMs to M1-like macrophages in vitro

Extensive data suggest that excess M2-like macrophages are one of the major factors in the progression of colorectal cancer metastasis [30]. It has been claimed that M2-like macrophages can promote tumor cell proliferation and metastasis and immunosuppression by increasing the levels of epidermal growth factor, matrix metalloproteinase (MMP), and vascular endothelial growth factor (VEGF), in addition to the secretion of cytokines [31–33]. In contrast, M1-like macrophages play an opposing role and directly kill tumor cells by secreting antitumor factors such as TNF α and IL-1β [34]. Hence, repolarizing TAMs into M1-like macrophages represents an important therapeutic approach. NO, a secondary signaling molecule, has been shown to effectively enhance the polarization of M1-like macrophages [9].

Afterward, we explored the polarization effect of PG/ICG@MP on TAMs in vitro. The polarization ability was examined through six well co-culture systems. MC38 cells were co-incubated with PBS, IL-4, LPS, and PG/ICG@MP in the bottom chamber, and RAW 264.7 cells were seeded in the upper chamber, after 24 h, the cellular morphology of RAW 264.7 was observed (Fig. S18). After that, RNA was isolated for RT-qPCR to confirm their polarization. LPS is a conventional drug used to induce M1-like macrophages, while IL-4 is capable of inducing M2-like macrophages, as depicted in Fig. 5A and B, the PG/ICG, and PG/ICG@MP treatment groups exhibited higher expression of M1-like macrophages markers (TNF α and iNOS) compared to the control group, while not displaying significant expression of M2-like macrophages markers (ARG1 and MRC1) (Fig. 5C, D). These findings indicated that TAMs treated with PG/ICG@MP could significantly upregulate M1-related markers TNF α and iNOS while downregulating M2-related markers ARG1 and MRC1.

Given that M2-like macrophages comprise the greatest number of TAM, the direct repolarizing effect of PG/ICG@MP on M2-like macrophages was then studied in vitro. RAW 264.7 cells were differentiated into M2-like macrophages by pre-treating them with IL-4 following the protocol described in reference [35]. After treated with different treatment groups, M1-like macrophage marker CD 80 was detected by Flow cytometry, as depicted in Fig. 5E and Fig. S19. In particular, the group treated with PG/ICG@MPs and irradiated with an 808 nm laser, exhibited the highest CD 80 expression, whereas the PBS group showed the lowest CD 80 expression. Furthermore, we utilized the Transwell system to investigate whether PG/ICG@MPs attract macrophages through chemotaxis. CCL2, a chemokine capable of stimulating macrophage migration, was utilized in our study. An 8-μm microporous membrane was employed to divide the layers, with RAW 264.7 cells cultured in the upper chamber and exposed to various treatments for 12 h. Among the groups tested, the PG/ICG@MP with MC38 cells exhibited the highest attraction of RAW 264.7 cells, as depicted in Fig. S20. These results indicated that PG/ICG@MPs could enhance the infiltration of macrophages. Thus, by effectively reprogramming TAMs to the M1 phenotype and increasing ROS and NO levels, PG/ICG@MPs have the potential to inhibit colorectal cancer cells.

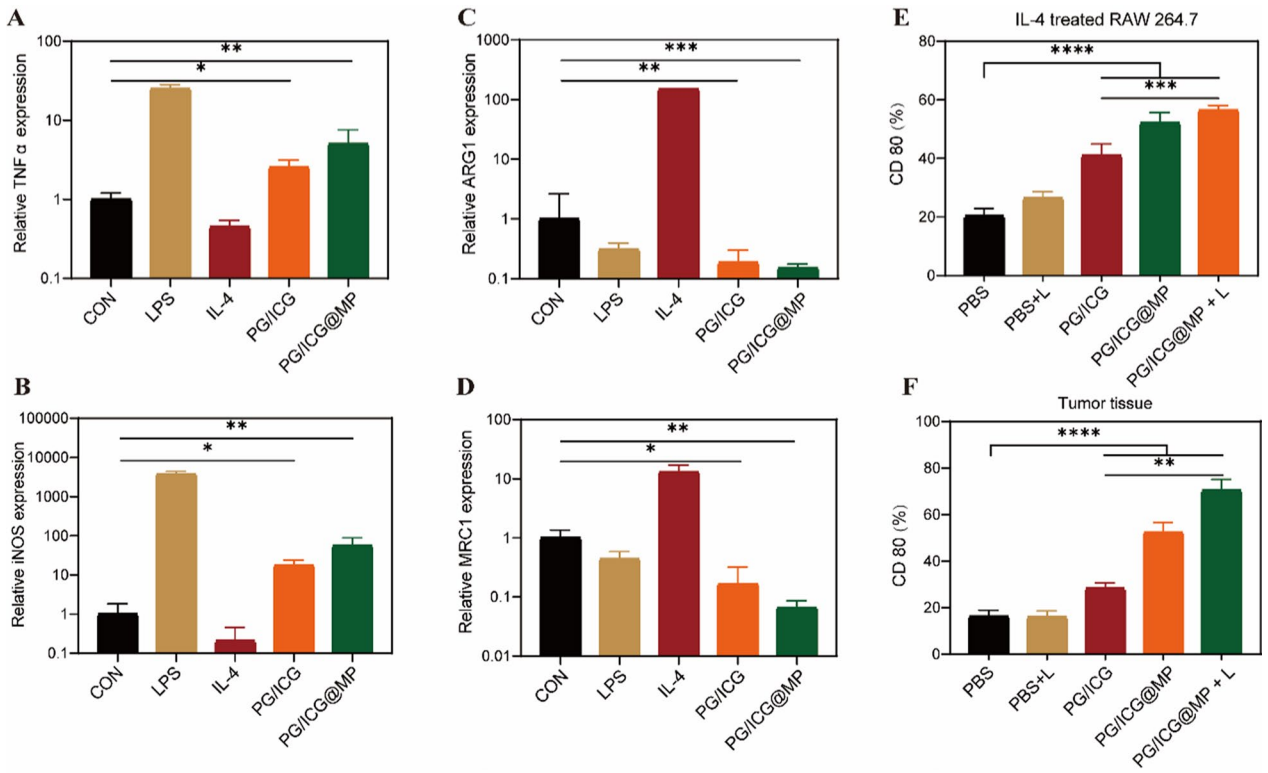

Fig. 5 PG/ICG@MPs could induce the repolarization of TAMs to the M1 phenotype to enhanced tumor immunity. **A**, **B** Quantification of TNF α and iNOS expression in different treatment groups using RT-qPCR. The PG/ICG@MP treatment group had higher proportion of TNF α and iNOS than the control group. **C**, **D** Quantification of ARG1 and MRC1 expression via RT—qPCR in different treatment groups. Compared with the control group, the PG/ICG@MP treatment group presented lower proportions of ARG1 and MRC1. **E** Expression of M1-like macrophage marker CD 80 in RAW 264.7 cells under different treatments. **F** Expression of M1-like macrophage marker CD 80 in tumor tissue from mice under different treatments. * $p < 0.05$, ** $p < 0.01$, *** $p < 0.001$, **** $p < 0.0001$

The effect of PG/ICG@MPs on xenograft tumors in vivo

Following in vitro validation, we investigated the antitumor activity of PG/ICG@MPs in vivo. As illustrated in Fig. 6A, the MC38 cells were subcutaneously inoculated into the right flank of the mouse to establish the tumor model. Once the tumor volume reached approximately 100 mm^3, PBS, PG/ICG, and PG/ICG@MP derived from MC38 cells were intravenously injected twice every 2 days, followed by treatment with or without 808 nm laser irradiation (1 W/cm^2, 10 min) at the tumor sites. In accordance with previous cell experiments, PG/ICG@MPs irradiated with 808 nm laser (PG/ICG@MP + L) demonstrated pronounced inhibition of tumor growth (Fig. 6B, Fig. S21) due to the strong photothermal therapy (PTT) effect of ICG. In contrast, the tumors in the PBS-treated group continued to grow, and the tumor weight in the PG/ICG@MP + L group was the lowest compared to other groups (Fig. 6C). Furthermore, none of the treatment groups experienced any prominent weight loss during the fifteen-day treatment period (Fig. 6D). The biochemical analysis of blood from mice in PBS and PG/ICG@MP treatment groups after 2 weeks (including aspartate aminotransferase (AST), alanine aminotransferase (ALT), alkaline phosphatase (ALP), lactate dehydrogenase (LDH), blood urea nitrogen (BUN), and creatinine (CREA) levels) revealed no significant changes, indicating that PG/ICG@MPs have no apparent toxicity in these mice (Fig. S22). Additionally, hematoxylin–eosin (HE) staining of the liver, kidney, and intestines revealed no significant differences between the two groups (Fig. S23). At the conclusion of the 40-day observation period, the combination treatment group demonstrated a generally higher survival rate compared to the control group, as shown in Fig. S24.

After treatment, we examined the changes in ARG1 and iNOS levels across the various treatment groups. One mouse from each treatment group was selected for sacrifice at fifteen days post-treatment, and tumor tissues were collected. Half of the tissues were used to extract single-cell suspensions, while the other half was subjected to HE staining and immunofluorescence analysis. As depicted in Fig. 6E, the PG/ICG@MP + L treatment group displayed a higher proportion of iNOS and a lower proportion of ARG1 (Fig. 6E), in contrast,

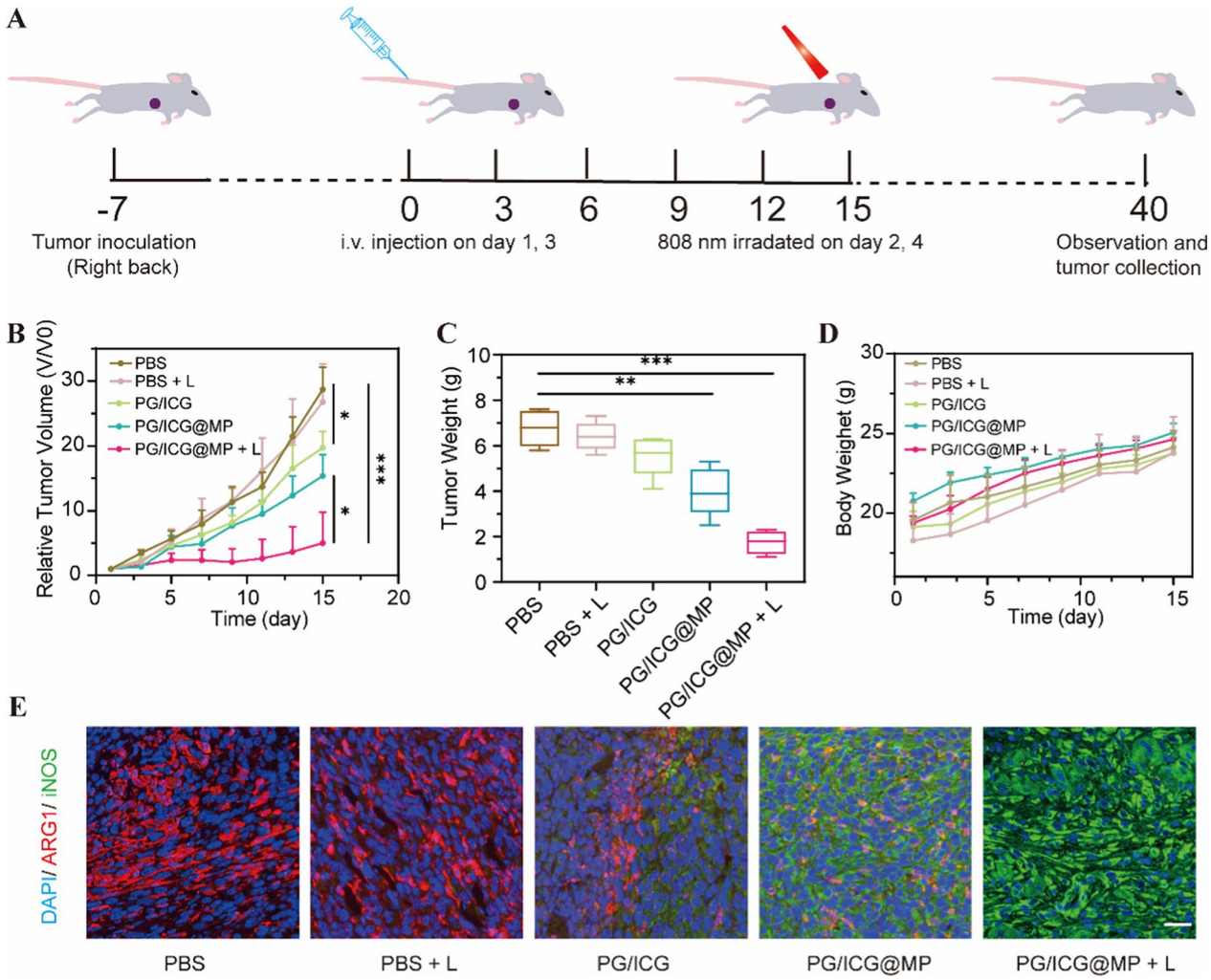

Fig. 6 In vivo therapeutic effect of PG/ICG@MPs. **A** Schematic illustration of the animal experiment. In summary, one week after the MC38 subcutaneous tumors was established, PG/ICG@MPs were administered via tail vein injection twice, with a one-day interval between injections. Each injection was followed by 808 nm laser irradiation at the tumor site 12 h later. The body weight, tumor volume, and survival of the mice in each group were monitored every two days until 40 days post-treatment. **B** Relative tumor volume in different treatment groups. **C** Tumor weights in different treatment groups. **D** Body weights of the mice in the different treatment groups. **E** Immunofluorescence detection of ARG1 (red), iNOS (green), and DAPI (blue) in tumor tissue from different treatment groups. Scale bar = 20 μm. * $p < 0.05$, ** $p < 0.01$, *** $p < 0.001$, **** $p < 0.0001$

the control group exhibited a notable ARG1 expression. Additionally, in Fig. 5F and Fig. S25, the percentage of M1-like macrophages in the PG/ICG@MP with 808 nm laser treatment group was notably high at 69%, whereas the PBS treatment group exhibited only 14.3% M1-like macrophages. Immunofluorescence analysis further confirmed a higher proportion of M1-like macrophages in the PG/ICG@MP with 808 nm laser treatment group (Fig. S26), In contrast, the control group exhibited a prominent presence of M2-like macrophages, known to promote tumor progression. TUNEL assays (Fig. S27) and HE staining (Fig. S28) showed that the PG/ICG@MP group treated with 808 nm irradiation achieved the best therapeutic outcomes.

Discussion

Abnormal arginine metabolism is common in tumors and is also a significant contributing factor to the increase in M2-like macrophages in the tumor microenvironment, thereby promoting the formation of an immunosuppressive microenvironment. Our results demonstrate that the recombinant microparticles PG/ICG@MPs target the elevated arginase levels in abnormal arginine metabolism, increasing the ratio of M1/M2 macrophages and enhancing antitumor immunity. Simultaneously, the PG-activated NOS enzyme promotes NO production, while when combined with ICG, it generates more ROS and high temperatures for tumor ablation, thereby exerting a certain inhibitory effect on tumors. Colorectal cancer

often exhibits abundant abnormal arginase, with a large number of M2-like macrophages in the tumor microenvironment, making colorectal cancer clinically insensitive to immunotherapy. Our study demonstrates the potential to stimulate the immune response in colorectal cancer and boost tumor-killing with abundant ROS, offering a hopeful outlook for enhancing clinical treatments for colorectal cancer.

Our previous bioinformatics analysis revealed that apart from being abundantly expressed in colorectal cancer [36], arginase is significantly elevated in other tumors such as pancreatic cancer [37], and prostate cancer [38]. Although our study focused on colorectal cancer cells and animal models, Moreover, due to the unique biological characteristics and metabolic differences of various types of tumors, arginase expression is abnormally elevated in only some malignant tumors [39]. These malignant tumors may share common target points. This recombinant microparticle may have similar effects on tumors with abnormal arginine metabolism, improving the immunosuppressive tumor microenvironment and enhancing tumor treatment outcomes.

EVs derived from cells represent a promising platform for drug delivery. Extensive research has delved into the field of EVs, which are generated from various sources such as tumor cells [40], mesenchymal stem cells [41], adipocytes [42, 43], macrophages [44], and T cells [45]. Although previous studies suggest that tumor cell-derived exosomes may transmit signals that promote tumor growth, subjecting tumor cells to physical or chemical stimuli, such as starvation or ultraviolet irradiation, may mitigate the pro-cancer effects of their secreted EVs [46]. Theoretically, tumor derived EVs can target not only the solid components of tumors but also circulating tumor cells (CTCs) in the bloodstream with potential specificity. While our study validated these findings only at the cellular and animal levels, considering the excellent biosafety of our recombinant microparticles, further clinical validation of recombinant EVs' application is necessary. Nevertheless, the transition from experimental to clinical stages still faces significant challenges. We anticipate that these intriguing recombinant microparticles will herald more effective cancer treatment strategies.

In summary, our study presents an exciting therapy to improve the tumor immune microenvironment. The recombinant PG/ICG@MPs modulate arginine metabolism in tumor tissue, increased the ratio of M1/M2 macrophages, and increased NO levels. When combined with ICG to generate more ROS, this approach exerts significant killing and inhibitory effects on tumors. With excellent biosafety and tumor-targeting capabilities, this strategy represents a promising clinical approach for cancer treatment.

Abbreviations

PG	Piceatannol 3′-*O*-glucoside
ICG	Indocyanine green
IM	ICG@MP
PM	PG@MP
PIM	PG/ICG@MP
TAM	Tumor-associated macrophage
MP	Cell microparticles
EV	Extracellular vesicles
PDT	Photodynamic therapy
PTT	Photothermal therapy
CTC	Circulating tumor cell
ARG	Arginase
NO	Nitric oxide
NOS	Nitric oxide synthase
iNOS	Inducible nitric oxide synthase
DC	Dendritic cell
ROS	Reactive oxygen species
FBS	Fetal bovine serum
PVDF	Polyvinylidene difluoride membranes
HE	Hematein–Eosin
IHC	Immunohistochemistry
MMP	Mitochondrial membrane potential
PFA	Paraformaldehyde

Supplementary Information

The online version contains supplementary material available at https://doi.org/10.1186/s12967-024-05652-3.

Additional file 1: Table S1. The series and company of primary antibodies. Table S2. The primer sequences used for qRT-PCR. Fig. S1.ARG1 expression in colorectal cancer tissue compared to adjacent normal tissue.ARG1 expression in various cancer cell lines. Fig. S2. 2D Chemical Structure Depiction of Piceatannol 3′-O-glucoside. Fig. S3. The anticancer effects of PG on colorectal cancer progression.Cell invasion and migration ability of two groups was measured with Transwell assays,Quantification of cell number in Figure 2A and 2C. * $p < 0.05$, ** $p < 0.01$, *** $p < 0.001$, **** $p < 0.0001$. Fig. S4.Cell proliferation ability of two groups was determined using CCK8 assays.Cell migration ability of two group was measured by Wound Healing assays. $p < 0.05$, ** $p < 0.01$, *** $p < 0.001$, **** $p < 0.0001$. Fig. S5. SW480, LoVo, and HCT116 cells were treated with PBS and PG. Annexin V - FITC was used to detect cell apoptosis, including early apoptosis, late apoptosis, dead cells, and living cells. The PG treatment group demonstrated a stronger tumor-killing effect compared to the control group. Fig. S6. SW480, LoVo, and HCT116 cells were treated with PBS and PG. CellTiter-Glo assays were conducted to measure cell proliferation across different treatment groups, and cell viability was calculated. The PG treatment group demonstrated a stronger tumor-killing effect compared to the control group. * p < 0.05, ** p < 0.01, *** p < 0.001, **** p < 0.0001. Fig. S7.Standard curve of ICG,Standard curve of PG. Fig. S8.Diameter of PG/ICG@MPs, PG/ICG@MPs, ICG@MPs, and MPs over a period of seven consecutive days, with no significant changes were observed.Zeta potential of PG/ICG@MPs, PG/ICG@MPs, ICG@MPs, and MP over a period of seven consecutive days, with no significant changes were observed. Fig. S9. In vivo fluorescence of MC38 subcutaneous tumor model in 0, 6, 12, 24, and 48 hours.Fig. S10. In vivo fluorescence of the heart, liver, spleen, kidney, and tumor at 12 hours.Fig. S11. Standard curve of total NO in cell tested by Griess assay. Fig. S12. Total NO in B16 and 786O cell lines treated with PGfor 24 h using Griess assay. * p < 0.05, ** p < 0.01, *** p < 0.001, **** p < 0.0001. Fig. S13. Mitochondrial membrane potential changes in LoVo cells with different treatments using JC-1 assay, bar = 100 μm. Fig. S14. Standard curve of ATP. Fig. S15. ATP concentration in LoVo cells co-incubated with different PG concentration, * p < 0.05, ** p < 0.01, *** p < 0.001, **** p < 0.0001.Fig. S16. MC38 Cell viability of different treatment groups. * p < 0.05, ** p < 0.01, *** p < 0.001, **** p < 0.0001. Fig. S17. Live and Dead cell staining by Calcein/ PI cell viability and cytotoxicity assay kit in PBS, PBS + L, PG/ICG, PG/ICG@MP, and PG/ICG@MP + L treatment group. Scale bar = 100 μm. Fig. S18. Photograph of RAW 264.7 after treated with PBS, IL-4, LPS, and PG/ICG@MP. Scale bar = 20 μm. Fig. S19. Detection of M1-like

macrophage markersin IL-4 treated RAW 264.7 macrophages of different groups by flow cytometry. Fig. S20.Photograph of RAW 264.7 which was recruited by PBS, CCL2, MC38, PG/ICG@MP, and MC38 + PG/ICG@MP by Transwell co-culture system, Scale bar = 50 μm.Cell number in different treatment groups, * $p < 0.05$, ** $p < 0.01$, *** $p < 0.001$, **** $p < 0.0001$. Fig. S21. Photograph of tumor tissue with different treatment groups. * $p < 0.05$, ** $p < 0.01$, *** $p < 0.001$, **** $p < 0.0001$. Fig. S22. Levels of AST, ALT, ALP, LDH, BUN, and CREA were measured in the blood serum of mice from both PBS and PG/ICG@MP treatment groups. The normal ranges for these biomarkers are as follows: AST, ALT, ALP, LDH, BUN, and CREA. * $p < 0.05$, ** $p < 0.01$, *** $p < 0.001$, **** $p < 0.0001$. Fig. S23. HE staining of the liver, kidney, and intestine sections from mice treated with PBS and PG/ICG@MP showed no pathological damage in either treatment group. Scale bar = 100 μm. Fig. S24. Survival rate of different treatment groups. Fig. S25. Detection of M1-like macrophage markerof tumor tissue from mice in different treatment groups tested by flow cytometry. Fig. S26. CD 80and CD 206were detected by Immunofluorescence of tumor tissue from mice in different treatment groups. Scale bar = 50 μm.Fig. S27. TUNEL assays of tumor tissue from mice in different treatment groups. Scale bar = 20 μm. Fig. S28. HE staining of tumor tissue from mice in different treatment groups. Scale bar = 100 μm.

Acknowledgements
We thank the financial support from National Natural Science Foundation of China, The Key Research and Development Project of Department of Science and Technology of Hubei, and The China Postdoctoral Science Foundation.

Author contributions
JW and KC conceived and designed the experiments. JW, SD and DC performed all the experiments. YC, JG and LQ analyzed the data. FM, YX and JZ prepared the figures. MC, FZ and NH contributed the reagents/materials/analysis tools. JW, SD and DC wrote the paper. KC revised the manuscript. All authors have read and approved the final manuscript.

Funding
This work is financially supported by the National Natural Science Foundation of China (No.82170678); The Key Research and Development Project of Department of Science and Technology of Hubei (No.2021BAA044); The China Postdoctoral Science Foundation (No. 2023M731216).

Availability of data and materials
The original contributions presented in the study are included in the article/Supplementary Material. Further inquiries can be directed to the corresponding authors.

Declarations

Ethics approval and consent to participate
The colorectal cancer tissue used in this work has been carried out in accordance with The Code of Ethics of the World Medical Association (Declaration of Helsinki). All patients provided signed informed consent and did not undergo adjuvant chemotherapy before surgery. The Human Research Ethics Committee of Huazhong University of Science and Technology approved our research. All animal studies were conducted in accordance with the guidelines of Tongji Medical College of Huazhong University of Science and Technology and were approved by the Animal Ethics Committee of Tongji Medical College of Huazhong University of Science and Technology. All animal experiments were performed in accordance with the National Research Council's Guide for the Care and Use of Laboratory Animals and the protocol was approved by the Institutional Animal Care and Use Committee, Tongji Medical College, Huazhong University of Science and Technology. (Approval number: S3366).

Consent for publication
Not application.

Competing interests
The authors declare that they have no known competing financial interests or personal relationships that could have appeared to influence the work reported in this paper.

Author details
[1]Gastrointestinal Surgery, Union Hospital, Tongji Medical College, Huazhong University of Science and Technology, Wuhan 430022, China. [2]Center for Liver Transplantation, Union Hospital, Tongji Medical College, Huazhong University of Science and Technology, Wuhan 430022, China. [3]Cancer Center, Union Hospital, Tongji Medical College, Huazhong University of Science and Technology, Wuhan 430022, China. [4]Departments of Diagnostic Radiology, Surgery, Chemical and Biomolecular Engineering, and Biomedical Engineering, Yong Loo Lin School of Medicine and College of Design and Engineering, National University of Singapore, Singapore 119074, Singapore. [5]Clinical Imaging Research Centre, Centre for Translational Medicine, Yong Loo Lin School of Medicine, National University of Singapore, Singapore 117599, Singapore.

Received: 19 June 2024 Accepted: 4 September 2024
Published online: 07 October 2024

References

1. Mellman I, Chen DS, Powles T, Turley SJ. The cancer-immunity cycle: indication, genotype, and immunotype. Immunity. 2023;56:2188–205.
2. Sharma P, Goswami S, Raychaudhuri D, Siddiqui BA, Singh P, Nagarajan A, Liu J, Subudhi SK, Poon C, Gant KL, et al. Immune checkpoint therapy-current perspectives and future directions. Cell. 2023;186:1652–69.
3. Pan Y, Yu Y, Wang X, Zhang T. Tumor-associated macrophages in tumor immunity. Front Immunol. 2020;11: 583084.
4. Biswas SK. Metabolic reprogramming of immune cells in cancer progression. Immunity. 2015;43:435–49.
5. Rodriguez PC, Ochoa AC, Al-Khami AA. Arginine metabolism in myeloid cells shapes innate and adaptive immunity. Front Immunol. 2017;8:93.
6. Katzenelenbogen Y, Sheban F, Yalin A, Yofe I, Svetlichnyy D, Jaitin DA, Bornstein C, Moshe A, Keren-Shaul H, Cohen M, et al. Coupled scRNA-Seq and intracellular protein activity reveal an immunosuppressive role of TREM2 in cancer. Cell. 2020;182:872-885.e819.
7. Pham TN, Liagre B, Girard-Thernier C, Demougeot C. Research of novel anticancer agents targeting arginase inhibition. Drug Discov Today. 2018;23:871–8.
8. Niu F, Yu Y, Li Z, Ren Y, Li Z, Ye Q, Liu P, Ji C, Qian L, Xiong Y. Arginase: an emerging and promising therapeutic target for cancer treatment. Biomed Pharmacother. 2022;149: 112840.
9. Palmieri EM, Gonzalez-Cotto M, Baseler WA, Davies LC, Ghesquière B, Maio N, Rice CM, Rouault TA, Cassel T, Higashi RM, et al. Nitric oxide orchestrates metabolic rewiring in M1 macrophages by targeting aconitase 2 and pyruvate dehydrogenase. Nat Commun. 2020;11:698.
10. Nath N, Kashfi K. Tumor associated macrophages and 'NO.' Biochem Pharmacol. 2020;176: 113899.
11. Wang X, Xiang H, Toyoshima Y, Shen W, Shichi S, Nakamoto H, Kimura S, Sugiyama K, Homma S, Miyagi Y, et al. Arginase-1 inhibition reduces migration ability and metastatic colonization of colon cancer cells. Cancer Metab. 2023;11:1.
12. Yao J, Du Z, Li Z, Zhang S, Lin Y, Li H, Zhou L, Wang Y, Yan G, Wu X, et al. 6-Gingerol as an arginase inhibitor prevents urethane-induced lung carcinogenesis by reprogramming tumor supporting M2 macrophages to M1 phenotype. Food Funct. 2018;9:4611–20.
13. Azambuja JH, Ludwig N, Yerneni SS, Braganhol E, Whiteside TL. Arginase-1+ exosomes from reprogrammed macrophages promote glioblastoma progression. Int J Mol Sci. 2020;21:3990.
14. Pudlo M, Demougeot C, Girard-Thernier C. Arginase inhibitors: a rational approach over one century. Med Res Rev. 2017;37:475–513.
15. Abdelkawy KS, Lack K, Elbarbry F. Pharmacokinetics and pharmacodynamics of promising arginase inhibitors. Eur J Drug Metab Pharmacokinet. 2017;42:355–70.

16. Gzik A, Borek B, Chrzanowski J, Jedrzejczak K, Dziegielewski M, Brzezinska J, Nowicka J, Grzybowski MM, Rejczak T, Niedzialek D, et al. Novel orally bioavailable piperidine derivatives as extracellular arginase inhibitors developed by a ring expansion. Eur J Med Chem. 2024;264: 116033.
17. Ivanenkov YA, Chufarova NV. Small-molecule arginase inhibitors. Pharm Pat Anal. 2014;3:65–85.
18. Woo A, Min B, Ryoo S. Piceatannol-3′-*O*-beta-D-glucopyranoside as an active component of rhubarb activates endothelial nitric oxide synthase through inhibition of arginase activity. Exp Mol Med. 2010;42:524–32.
19. Woo A, Shin W, Cuong TD, Min B, Lee JH, Jeon BH, Ryoo S. Arginase inhibition by piceatannol-3′-*O*-β-D-glucopyranoside improves endothelial dysfunction via activation of endothelial nitric oxide synthase in ApoE-null mice fed a high-cholesterol diet. Int J Mol Med. 2013;31:803–10.
20. Chiou YS, Lan YM, Lee PS, Lin Q, Nagabhushanam K, Ho CT, Pan MH. Piceatannol prevents colon cancer progression via dual-targeting to M2-polarized tumor-associated macrophages and the TGF-β1 positive feedback signaling pathway. Mol Nutr Food Res. 2022;66: e2200248.
21. van Niel G, D'Angelo G, Raposo G. Shedding light on the cell biology of extracellular vesicles. Nat Rev Mol Cell Biol. 2018;19:213–28.
22. Xu R, Greening DW, Zhu HJ, Takahashi N, Simpson RJ. Extracellular vesicle isolation and characterization: toward clinical application. J Clin Invest. 2016;126:1152–62.
23. Elsharkasy OM, Nordin JZ, Hagey DW, de Jong OG, Schiffelers RM, Andaloussi SE, Vader P. Extracellular vesicles as drug delivery systems: Why and how? Adv Drug Deliv Rev. 2020;159:332–43.
24. Herrmann IK, Wood MJA, Fuhrmann G. Extracellular vesicles as a next-generation drug delivery platform. Nat Nanotechnol. 2021;16:748–59.
25. Escudier B, Dorval T, Chaput N, André F, Caby MP, Novault S, Flament C, Leboulaire C, Borg C, Amigorena S, et al. Vaccination of metastatic melanoma patients with autologous dendritic cell (DC) derived-exosomes: results of the first phase I clinical trial. J Transl Med. 2005;3:10.
26. Besse B, Charrier M, Lapierre V, Dansin E, Lantz O, Planchard D, Le Chevalier T, Livartoski A, Barlesi F, Laplanche A, et al. Dendritic cell-derived exosomes as maintenance immunotherapy after first line chemotherapy in NSCLC. Oncoimmunology. 2016;5: e1071008.
27. Zipprich A, Kuss O, Rogowski S, Kleber G, Lotterer E, Seufferlein T, Fleig WE, Dollinger MM. Incorporating indocyanin green clearance into the Model for End Stage Liver Disease (MELD-ICG) improves prognostic accuracy in intermediate to advanced cirrhosis. Gut. 2010;59:963–8.
28. Bailey JD, Diotallevi M, Nicol T, McNeill E, Shaw A, Chuaiphichai S, Hale A, Starr A, Nandi M, Stylianou E, et al. Nitric oxide modulates metabolic remodeling in inflammatory macrophages through TCA cycle regulation and itaconate accumulation. Cell Rep. 2019;28:218-230.e217.
29. Deng Y, Jia F, Chen X, Jin Q, Ji J. ATP suppression by pH-activated mitochondria-targeted delivery of nitric oxide nanoplatform for drug resistance reversal and metastasis inhibition. Small. 2020;16: e2001747.
30. Li R, Zhou R, Wang H, Li W, Pan M, Yao X, Zhan W, Yang S, Xu L, Ding Y, Zhao L. Gut microbiota-stimulated cathepsin K secretion mediates TLR4-dependent M2 macrophage polarization and promotes tumor metastasis in colorectal cancer. Cell Death Differ. 2019;26:2447–63.
31. Mehla K, Singh PK. Metabolic regulation of macrophage polarization in cancer. Trends Cancer. 2019;5:822–34.
32. Locati M, Curtale G, Mantovani A. Diversity, mechanisms, and significance of macrophage plasticity. Annu Rev Pathol. 2020;15:123–47.
33. Wang H, Yung MMH, Ngan HYS, Chan KKL, Chan DW. The impact of the tumor microenvironment on macrophage polarization in cancer metastatic progression. Int J Mol Sci. 2021;22:6560.
34. Wu MF, Lin CA, Yuan TH, Yeh HY, Su SF, Guo CL, Chang GC, Li KC, Ho CC, Chen HW. The M1/M2 spectrum and plasticity of malignant pleural effusion-macrophage in advanced lung cancer. Cancer Immunol Immunother. 2021;70:1435–50.
35. Kulkarni A, Chandrasekar V, Natarajan SK, Ramesh A, Pandey P, Nirgud J, Bhatnagar H, Ashok D, Ajay AK, Sengupta S. A designer self-assembled supramolecule amplifies macrophage immune responses against aggressive cancer. Nat Biomed Eng. 2018;2:589–99.
36. Ma Z, Lian J, Yang M, Wuyang J, Zhao C, Chen W, Liu C, Zhao Q, Lou C, Han J, Zhang Y. Overexpression of Arginase-1 is an indicator of poor prognosis in patients with colorectal cancer. Pathol Res Pract. 2019;215: 152383.
37. Menjivar RE, Nwosu ZC, Du W, Donahue KL, Hong HS, Espinoza C, Brown K, Velez-Delgado A, Yan W, Lima F, et al. Arginase 1 is a key driver of immune suppression in pancreatic cancer. Elife. 2023;12: e80721.
38. Mumenthaler SM, Yu H, Tze S, Cederbaum SD, Pegg AE, Seligson DB, Grody WW. Expression of arginase II in prostate cancer. Int J Oncol. 2008;32:357–65.
39. Caldwell RW, Rodriguez PC, Toque HA, Narayanan SP, Caldwell RB. Arginase: a multifaceted enzyme important in health and disease. Physiol Rev. 2018;98:641–65.
40. Taghikhani A, Farzaneh F, Sharifzad F, Mardpour S, Ebrahimi M, Hassan ZM. Engineered tumor-derived extracellular vesicles: potentials in cancer immunotherapy. Front Immunol. 2020;11:221.
41. Weng Z, Zhang B, Wu C, Yu F, Han B, Li B, Li L. Therapeutic roles of mesenchymal stem cell-derived extracellular vesicles in cancer. J Hematol Oncol. 2021;14:136.
42. Kulaj K, Harger A, Bauer M, Caliskan ÖS, Gupta TK, Chiang DM, Milbank E, Reber J, Karlas A, Kotzbeck P, et al. Adipocyte-derived extracellular vesicles increase insulin secretion through transport of insulinotropic protein cargo. Nat Commun. 2023;14:709.
43. Zhang Q, Deng T, Zhang H, Zuo D, Zhu Q, Bai M, Liu R, Ning T, Zhang L, Yu Z, et al. Adipocyte-derived exosomal MTTP suppresses ferroptosis and promotes chemoresistance in colorectal cancer. Adv Sci (Weinh). 2022;9: e2203357.
44. Gunassekaran GR, Poongkavithai Vadevoo SM, Baek MC, Lee B. M1 macrophage exosomes engineered to foster M1 polarization and target the IL-4 receptor inhibit tumor growth by reprogramming tumor-associated macrophages into M1-like macrophages. Biomaterials. 2021;278: 121137.
45. Jung D, Shin S, Kang SM, Jung I, Ryu S, Noh S, Choi SJ, Jeong J, Lee BY, Kim KS, et al. Reprogramming of T cell-derived small extracellular vesicles using IL2 surface engineering induces potent anti-cancer effects through miRNA delivery. J Extracell Vesicles. 2022;11: e12287.
46. Hu Y, Sun Y, Wan C, Dai X, Wu S, Lo PC, Huang J, Lovell JF, Jin H, Yang K. Microparticles: biogenesis, characteristics and intervention therapy for cancers in preclinical and clinical research. J Nanobiotechnology. 2022;20:189.

Publisher's Note